



Microwave-assisted hydrothermal synthesis of Sn_3O_4 nanosheet/rGO planar heterostructure for efficient photocatalytic hydrogen generation

Xin Yu^a, Zhenhuan Zhao^b, Dehui Sun^{a,*,**}, Na Ren^a, Jinghua Yu^a, Ruiqi Yang^a, Hong Liu^{a,c,*}

^a Institute for Advanced Interdisciplinary Research, University of Jinan, Jinan, 250022, PR China

^b School of Advanced Materials and Nanotechnology, Xidian University, 710071, PR China

^c State Key Laboratory of Crystal Materials, Shandong University, Jinan, 250100, PR China



ARTICLE INFO

Keywords:
Photocatalysis
 H_2 generation
 Sn_3O_4 /rGO
Heterostructure
Microwave-assisted hydrothermal

ABSTRACT

The present work reports the facile synthesis of a planar heterostructure consisted of Sn_3O_4 nanosheet and 2-dimentional reduced graphene oxide (rGO) through microwave-assisted hydrothermal method (MHM). The planar heterostructure features with extended light absorption range and shortened charge transfer distance, and hence exhibits excellent photocatalytic activity and stability, with a hydrogen evolution rate of 20 mmol/g/h. The photoelectrochemical characterization shows that the planar heterostructure has better charge separation efficiency and interfacial charge transfer kinetics, which are also demonstrated by photoluminescence (PL) spectra and time-resolved PL decay analysis. It is found that the lifetimes of the photocarriers increased in the heterostructure. This work provides a new design of planar heterostructure for photocatalytic hydrogen generation through facile synthesis.

1. Introduction

Hydrogen is a green fuel with high energy density and has been known as the potential alternative to fossil fuels [1–3]. Solar driven photocatalytic water splitting for hydrogen production has been considered as one of the most important approaches to solving the word energy crisis [4–9].

Recent years, tremendous efforts have been made for the development of novel and active photocatalysts to efficiently improve the solar to hydrogen conversion efficiency [10–14]. At least two main approaches have been developed. The first one is to design and fabricate narrow bandgap photocatalysts to extend the light absorption edge to visible range, and even to near infrared range [15–17]. The second one is to engineer the charge separation and transportation to maximize the number of photogenerated charges flowing to the catalyst surface for catalytic reaction [18–21]. However, narrow bandgap photocatalysts either suffer from serious photocorrosion or lack sufficient driven force for catalytic reaction because of their band positions [22]. Up to date, there is no single-phase photocatalyst that can efficiently drive the solar water splitting reaction because the fast recombination and poor charge separation. Heterostructured nanomaterials have been demonstrated to be effective photocatalysts capable of high stability, efficient charge separation and suppressed charge recombination, and hence exhibit

outstanding photocatalytic performance [23–27].

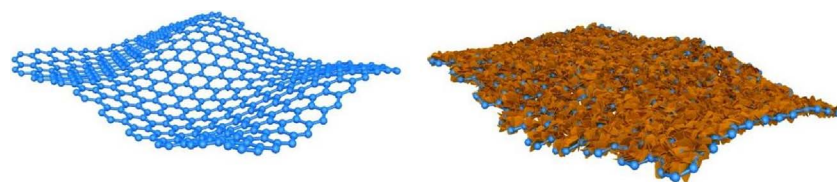
Tin oxides have been known as active photocatalysts due to the eco-friendly and earth-abundant features [28]. SnO_2 is not appropriate to drive the overall water splitting and commonly used as the photocatalyst catalyzing the oxygen evolution reaction because the conduction band position is typically lower than the water reduction potential while the valence band position is far lower than the water oxidation potential [29,30]. However, Sn_3O_4 has been found to be capable of photocatalytically splitting water to generate hydrogen [31–33]. However, the stability and performance is not satisfactory due to the poor charge separation and high recombination of the photoproduced electron and hole pairs. Reduced graphene oxide (rGO) has high surface area and high electrical conductivity, and hence widely used to be coupled with various semiconductor photocatalysts [34–36]. Typically, rGO is *in situ* reduced from graphene oxide (GO) during the synthetic process [37,38]. Since GO can be easily dispersed into various solvents and has high surface area, the coupled semiconductor nanostructures usually can have uniform distribution on the surface of rGO [39,40]. rGO has high electrical conductivity, and hence is the high speedway of electron transfer. It has been reported that coupling rGO with a semiconductor can extend the charge carrier lifetime, and hence enhances the photocatalytic activity [41–43].

Here, for the first time we report the facile one-pot synthesis of

* Corresponding author at: Institute for Advanced Interdisciplinary Research, University of Jinan, Jinan, 250022, PR China.

** Corresponding author.

E-mail addresses: ifc_sundh@ujn.edu.cn (D. Sun), ifc_liuh@ujn.edu.cn (H. Liu).



planar heterostructure consisted of rGO and Sn_3O_4 nanosheets through microwave-assisted hydrothermal method (Scheme 1). The planar heterostructure can efficiently drive the solar water splitting to generate hydrogen. The rGO cannot only increase the light absorbance, but also enhance the separation of photogenerated electron/hole pairs. This work provides a promising route for the future development of active heterostructure photocatalyst for clean fuels generation.

2. Results and discussion

The Sn_3O_4 /rGO planar heterostructure was synthesized by microwave-assisted hydrothermal method (MHM). MHM has the advantages of homogeneous mixing of the precursors at the molecular scale, fast heating speed without uniform temperature gradient, accelerated reaction kinetics and energy saving. Compared to the traditional hydrothermal method, one of the major merits is the reaction time can be significantly shortened by MHM, for example, in this case, from 12 h to 4 h. The morphology of the as-prepared samples was characterized by scanning electron microscope (SEM), as shown in Fig. 1. Sn_3O_4 shows 3D flower-like microstructure consisted of densely assembled

nanosheets (Fig. 1a and b). The SEM images of rGO are shown in Fig. 1c and 1d, which displays the typical 2D morphology of rGO. Microwave reduction can go to more oxygen-containing functional groups [44,45]. As it can be seen from the SEM images in Fig. 1e and f, the Sn_3O_4 nanosheets are uniformly decorated on rGO sheet. The average diameter of the Sn_3O_4 nanosheets is measured to be 150 nm.

The Sn_3O_4 microflower and the Sn_3O_4 /rGO planar heterostructure were further characterized by transmission electron microscopy (TEM). Fig. 2a shows the edge of the Sn_3O_4 microflower that consists of nanosheets having an average thickness of 20 nm. HRTEM image in Fig. 2b shows clear crystalline lattice suggesting the high crystallinity of Sn_3O_4 nanosheet. The measured lattice fringe spacing of 0.276 nm, 0.282 nm and 0.329 nm can be assigned to $(\bar{1}21)$, $(\bar{2}10)$ and (111) plane [46]. The TEM images in Fig. 2c and d show that the Sn_3O_4 nanosheets with a size of 150 nm were uniformly and parallel to on the rGO sheets to form a planar heterostructure. The planar heterostructure will short the distance of charge transfer between Sn_3O_4 and rGO. The selected area electron diffraction (SAED) image of the Sn_3O_4 /GO planar heterostructure shows a ring pattern corresponding to the (101) , (111) , $(\bar{1}21)$, (130) , $(\bar{3}01)$, $(\bar{1}32)$, (241) , (042) and (312) planes of Sn_3O_4 [47].

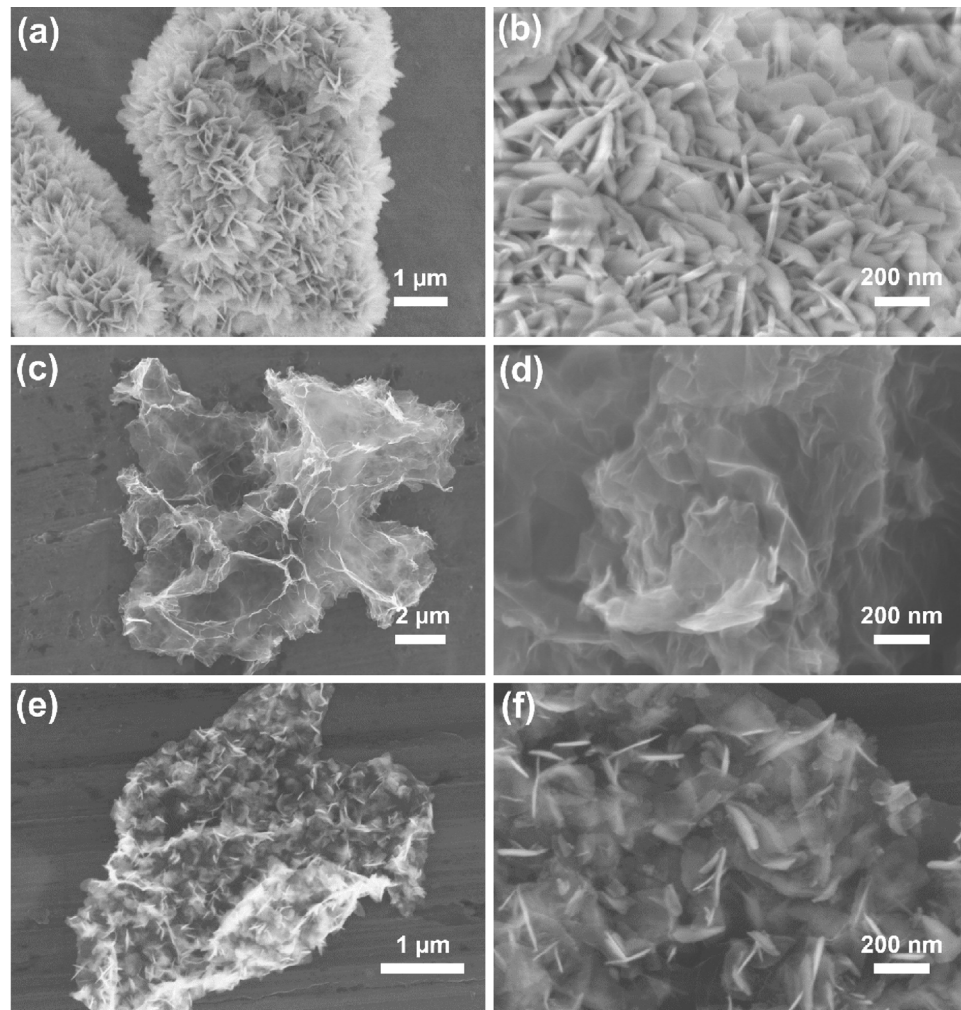


Fig. 1. Typical SEM images of (a, b) Sn_3O_4 nanosheet, (c, d) rGO nanosheet, (e, f) Sn_3O_4 /rGO heterostructure at different magnifications.

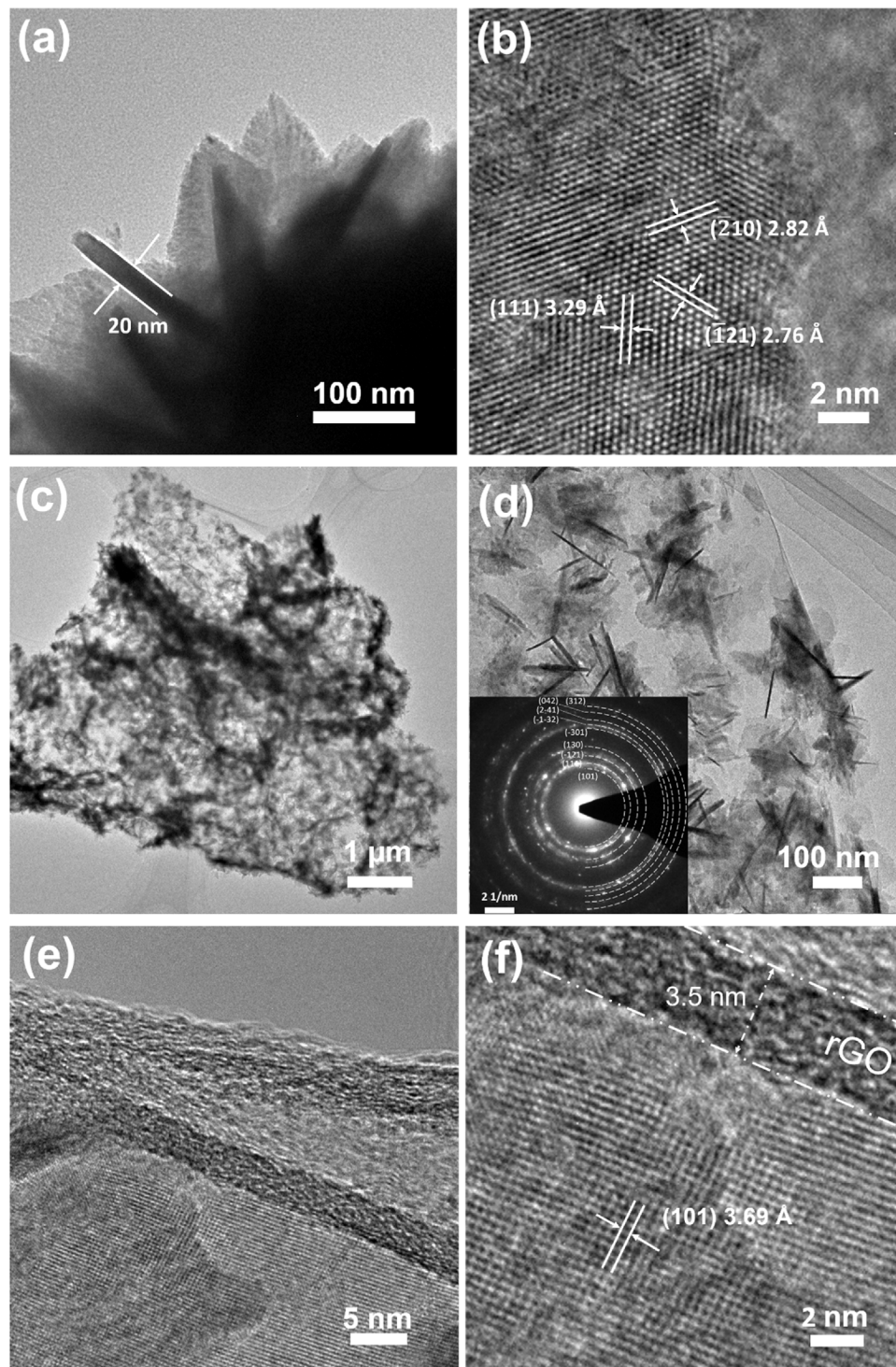


Fig. 2. (a, b) Typical TEM image and HRTEM image of Sn_3O_4 nanosheet, (c–f) Typical TEM images and HRTEM images of $\text{Sn}_3\text{O}_4/\text{rGO}$ heterostructure.

The HRTEM images in Fig. 2e and f further confirm the (101) plane of Sn_3O_4 given the fringe spacing of 0.369 nm. The thickness of the rGO is about 3.5 nm. Both the SEM and TEM results indicate the successful formation of the planar heterostructure between Sn_3O_4 nanosheet and rGO.

Fig. 3a shows the powder X-ray diffraction (XRD) patterns of the $\text{Sn}_3\text{O}_4/\text{rGO}$ planar heterostructure which matches well with standard diffraction patterns of PDF-#16-0737.[31] Due to low mass loading of rGO, the characteristic peaks of rGO cannot be observed. Raman spectra of Sn_3O_4 and $\text{Sn}_3\text{O}_4/\text{rGO}$ planar heterostructure in Fig. 3b indicates the existence of rGO given the peaks at 1580 and 1338 cm^{-1} corresponding

to characteristic vibration modes of the D and G bands of rGO [48].

The light absorption capability of Sn_3O_4 and $\text{Sn}_3\text{O}_4/\text{rGO}$ heterostructure are also investigated. Fig. 3c illustrates the UV-vis DRS spectra of Sn_3O_4 and $\text{Sn}_3\text{O}_4/\text{rGO}$ heterostructure. For pure Sn_3O_4 nanosheets, the light absorption edge is about 500 nm, located in the visible light range. While for the $\text{Sn}_3\text{O}_4/\text{rGO}$ heterostructure, the absorption spectra has a light absorption edge of about 600 nm and a tail after the edge which means the heterostructure can absorb more solar energy. The Tauc plots [49] in Fig. 3d suggest that Sn_3O_4 has indirect band gap of about 2.55 eV.

The chemical states of the heterostructure as well as pure Sn_3O_4

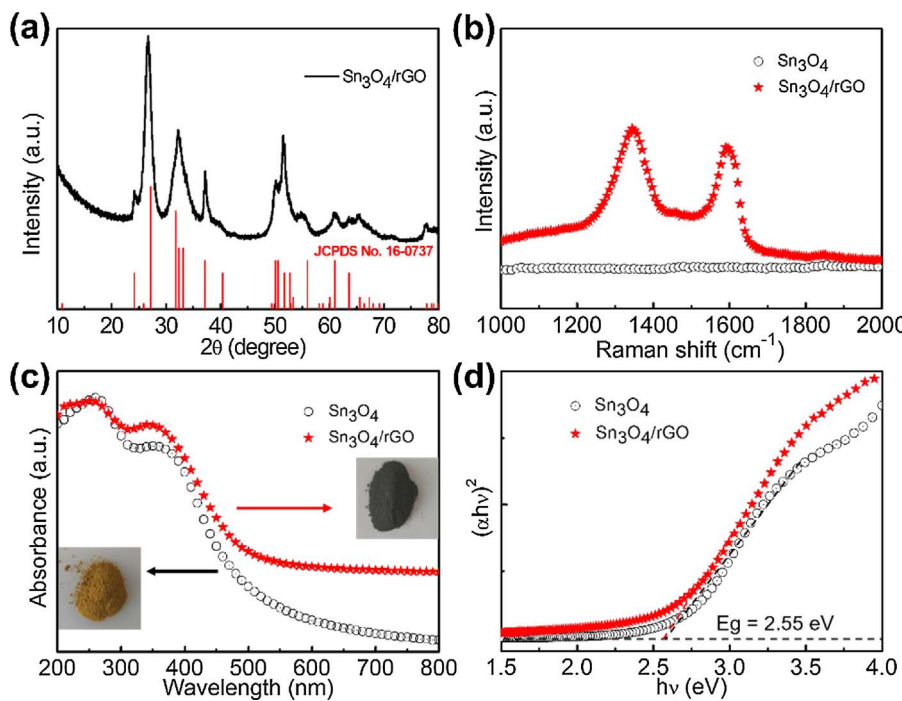


Fig. 3. (a) XRD patterns of $\text{Sn}_3\text{O}_4/\text{rGO}$ planar heterostructure. (b) Raman spectra of Sn_3O_4 nanosheets, $\text{Sn}_3\text{O}_4/\text{rGO}$ heterostructure excited by a 532 nm laser. (c) UV-vis diffuse reflectance spectra of Sn_3O_4 and $\text{Sn}_3\text{O}_4/\text{rGO}$ heterostructures. Inset: Digital photograph of the $\text{Sn}_3\text{O}_4/\text{rGO}$ fine powder catalyst. (d) Tauc plots of Sn_3O_4 and $\text{Sn}_3\text{O}_4/\text{rGO}$ heterostructure.

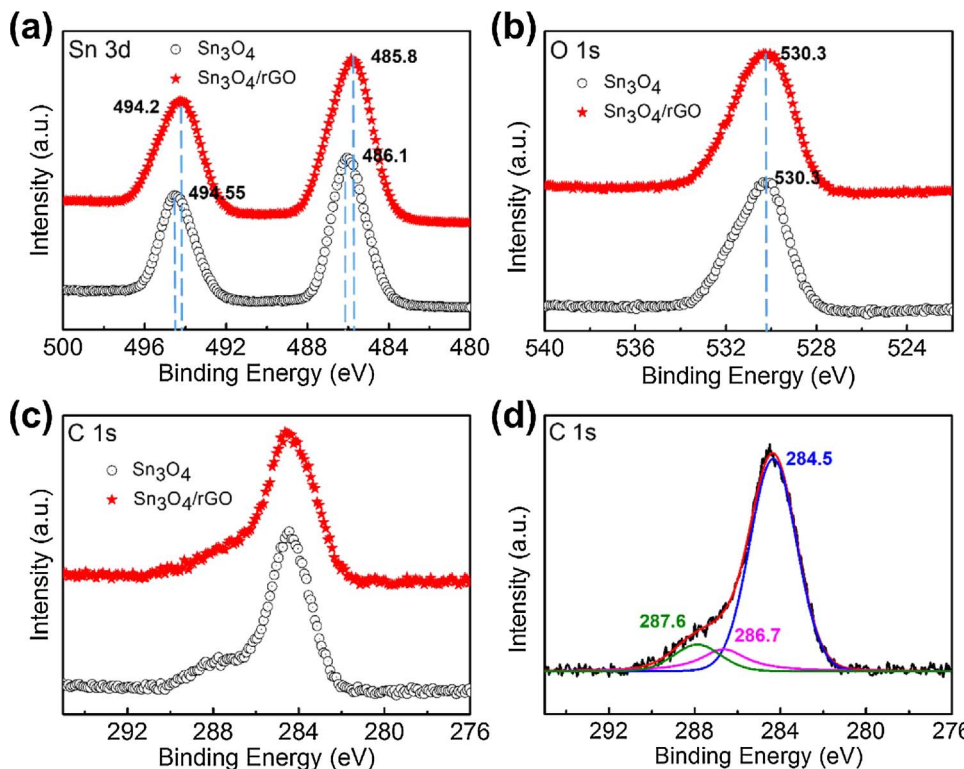


Fig. 4. XPS characterization of Sn_3O_4 and $\text{Sn}_3\text{O}_4/\text{rGO}$: (a) Sn 3d, (b) O 1s, (c) C 1s. (d) Fitting results of the C 1s for the $\text{Sn}_3\text{O}_4/\text{rGO}$ heterostructure.

were characterized by X-ray photoelectron spectroscopy (XPS), as shown in Fig. 4. The survey scan spectra in Fig. S2 indicates the presence of Sn, O, and C in $\text{Sn}_3\text{O}_4/\text{rGO}$ heterostructure. For pure Sn_3O_4 nanosheets, the Sn 3d spectra shows two peaks of Sn 3d_{5/2} and 3d_{3/2} located at 494.6 eV and 486.1 eV, while for the heterostructure these two peaks shift to lower binding energies of 494.2 eV and 485.8 eV. The chemical state of O in pure Sn_3O_4 and the heterostructure is the same with each other (Fig. 4b), which means the residual O in rGO has no effect on the chemical state of Sn. Therefore, the shift of the binding energy of Sn 3d suggests the charge transfer between Sn_3O_4 and rGO in

the heterostructure. The C 1s core level spectra was deconvoluted into three components (Fig. 4d) of the sp² carbon (284.5 eV), C–OH or –C–COOH (286.7 eV) and C=O (287.6 eV), respectively [50]. By comparing C 1s spectrum (Table S1) in Sn_3O_4 (Fig. 4d) and $\text{Sn}_3\text{O}_4/\text{rGO}$ (Fig. S3), The predominance of the sp² carbon contribution indicates that most oxygenated groups on GO sheets were efficiently removed by the hydrothermal reduction process, in good agreement with previous reports on rGO fabrication.

The photocatalytic activities of the as-prepared Sn_3O_4 nanosheets and $\text{Sn}_3\text{O}_4/\text{rGO}$ planar heterostructure were evaluated in suspension

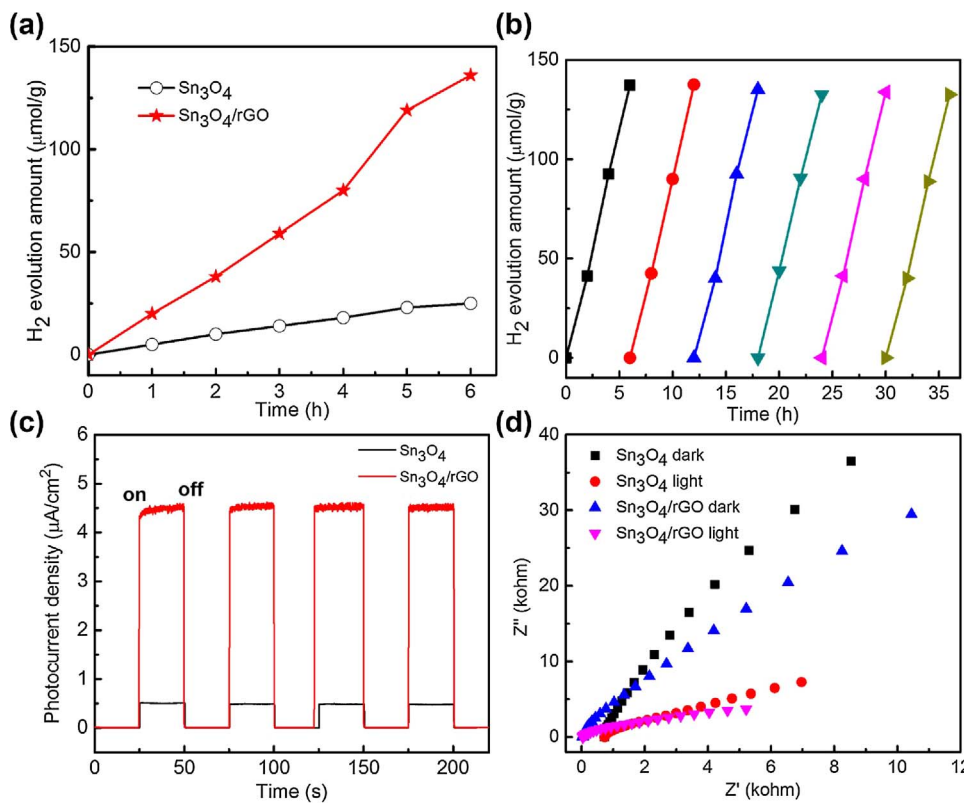


Fig. 5. (a) Photocatalytic hydrogen generation of Sn₃O₄ and Sn₃O₄/rGO heterostructure. (b) Photocatalytic H₂ evolution in 6 repeated cycles (6 h/cycle) by the Sn₃O₄/rGO heterostructure. Photoelectrochemical characterization: (c) ON-OFF curves of the Sn₃O₄ nanosheets and the Sn₃O₄/rGO heterostructure under light irradiation (bias voltage 0.1 V). (d) EIS Nyquist plots of the Sn₃O₄ and Sn₃O₄/rGO at a bias of 0 V in the dark and with light.

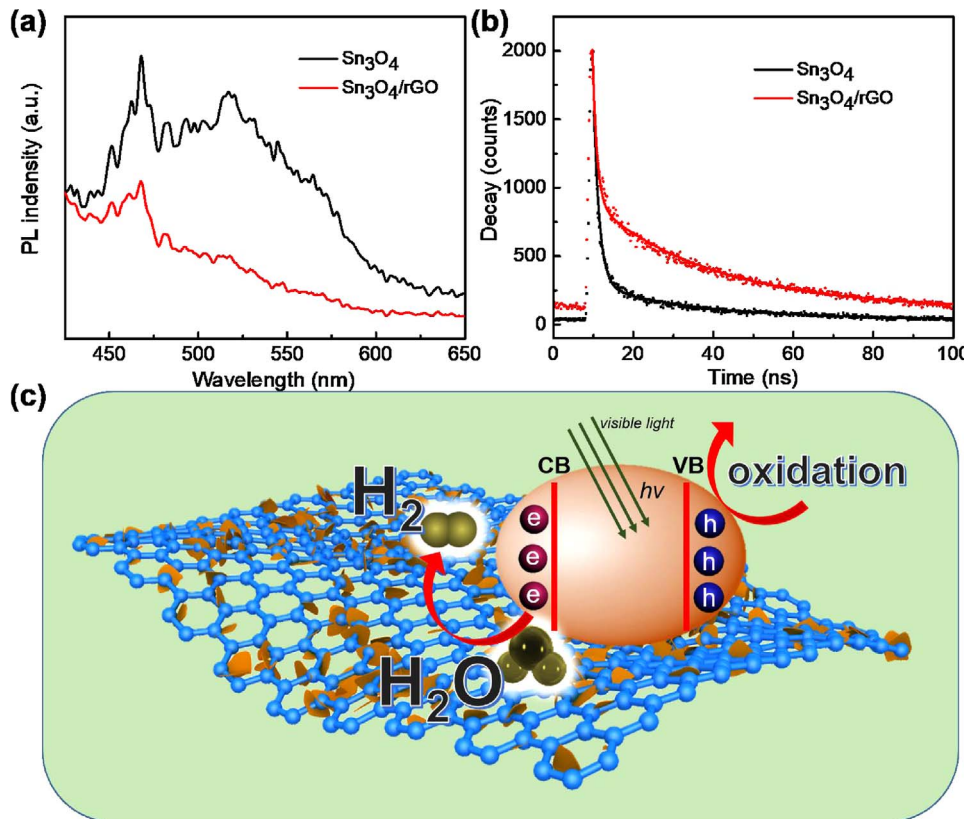


Fig. 6. (a) PL emission and (b) time-resolved PL decay spectra of the Sn₃O₄ and Sn₃O₄/rGO at 450 nm excited by a 375 nm laser at room temperature. (c) Schemes illustrating the transfer of charge carriers in aqueous solution over the Sn₃O₄/rGO heterostructure under visible light irradiation ($\lambda > 420$ nm).

system under visible light ($\lambda > 420$ nm) irradiation with ethanol as the sacrificial agent. Fig. 5 shows the curves of H₂ evolution amount as a function of irradiation time. As shown in Fig. 5a, the amount of evolved H₂ increases linearly with the irradiation time over 6 h for both Sn₃O₄

nanosheets and Sn₃O₄/rGO heterostructure. The hydrogen evolution rate (turnover number) of pure Sn₃O₄ is 4 mmol/h/g, while the heterostructure has a much higher rate of 20 mmol/h/g, a 5-fold enhancement. In addition, the heterostructure photocatalyst also exhibits

excellent stability as evidenced by the constant hydrogen evolution rate for the 1st cycle and the 6th cycle (Fig. 5b). The stability of Sn_3O_4 is poor. The hydrogen evolution of the 2nd cycle was significantly reduced. There is almost no hydrogen produced at the 4th cycle (Fig. S4).

Photoelectrochemical measurements were conducted to investigate the charge transfer mechanism of the as-prepared photocatalysts using a three-electrode configuration [51]. Fig. 5c shows the ON-OFF photocurrent curves of Sn_3O_4 nanosheets and the $\text{Sn}_3\text{O}_4/\text{rGO}$ heterostructure. Both samples display fast response to the visible light irradiation. As a result, the heterostructure shows a photocurrent density of 4.5 mA/cm^2 , an almost 9-fold enhancement compared to 0.45 mA/cm^2 of Sn_3O_4 , which is consistent with the trend seen in their photocatalytic hydrogen evolution activities. The much higher photocurrent measured for $\text{Sn}_3\text{O}_4/\text{rGO}$ heterostructure reflects a better visible light response and more efficient photoexcited charge separation compared with pure Sn_3O_4 nanosheets. Nyquist plots derived from the electrochemical impedance spectroscopy (EIS) are shown in Fig. 5d. The $\text{Sn}_3\text{O}_4/\text{rGO}$ heterostructure shows smaller semicircles both in the dark and under illumination than Sn_3O_4 nanosheets which indicates that the $\text{Sn}_3\text{O}_4/\text{rGO}$ heterostructure has faster interfacial electron transfer kinetics because of the high conductivity of rGO. It is concluded that by coupling rGO with Sn_3O_4 nanosheets to form planar heterostructure can promote the charge separation and prohibit the charge recombination, and can also facilitate the interfacial charge transfer.

More close investigation to the kinetics of the photogenerated electrons and holes was conducted by photoluminescence (PL) characterization and time-resolved PL decay measurements [52,53], as shown in Fig. 6. The $\text{Sn}_3\text{O}_4/\text{rGO}$ heterostructure shows much lower intensity of the emission peak compared to Sn_3O_4 nanosheets in the same wavelength range (Fig. 6a), indicating that the recombination of photoinduced electrons and holes is significantly prohibited. The charge separation efficiency was further analyzed by time-resolved PL decay spectra (Fig. 6b). The PL decay profiles can be fitted by bi-exponential equation, suggesting the two relaxation pathways of the photocarriers [54]. Table S2 summarizes the decay times, relative amplitude and average lifetimes of Sn_3O_4 nanosheets and the $\text{Sn}_3\text{O}_4/\text{rGO}$ heterostructure. It is found that the planar heterostructure (28.02 ns) shows longer lifetime than Sn_3O_4 nanosheets (25.71 ns), indicating that charge separation efficiency in the $\text{Sn}_3\text{O}_4/\text{rGO}$ heterostructure is improved and the recombination of photoinduced electron–hole pairs is suppressed. The planar heterostructure will shorten the pathway of charge transportation. As a consequence, more photoinduced electrons and holes can migrate to the catalyst surface responsible for the catalytic reactions to hydrogen evolution and ethanol oxidation.

Based on the above results, the high H_2 evolution activity of $\text{Sn}_3\text{O}_4/\text{rGO}$ heterostructure under visible light irradiation can be explained from the scheme of Fig. 6c. Under visible light irradiation, photo-generated holes and electrons appear in the valence bands (VB) and conduction bands (CB) of Sn_3O_4 . Normally, these charge carriers recombine rapidly resulting in a low photocatalytic H_2 evolution rate of Sn_3O_4 itself. However, when Sn_3O_4 nanoparticles are immobilized on the surface of rGO, those photogenerated electrons in CB of Sn_3O_4 tend to transfer to rGO, leading to the hole-electron separation. The rGO can function as an electron collector and transporter to lengthen the lifetime of the charge carriers, consequently improving the charge separation and photocatalytic activity. Furthermore, the high surface area of the planar heterostructure will also expose more catalytic active sites to the reaction molecules like water and ethanol. The present study provides a fast and simple synthetic method for high performance photocatalyst for the generation of clean fuels from solar energy.

3. Conclusions

In conclusion, the present study reported the facile synthesis of a planar heterostructure consisted of Sn_3O_4 nanosheets and rGO by

microwave-assisted hydrothermal method. The planar heterostructure is characterized by SEM, TEM, Raman and XPS. It is found that the microwave-assisted hydrothermal method can significantly shorten the reaction time and the Sn_3O_4 nanosheets can uniformly be grown on rGO. The heterostructure photocatalyst exhibits outstanding catalytic performance toward hydrogen evolution at a rate of 20 mmol/g/h . Photoelectrochemical measurements shows that the photocurrent density of the heterostructure is almost 10 times higher than pure Sn_3O_4 nanosheets, and also has much faster interfacial charge transfer kinetics. The mechanism of the charge separation was further investigated by PL and PL decay measurements which shows that the carrier lifetimes increased in the planar heterostructure. This facile synthesis method provides a general methodology for the preparation of photocatalytic graphene semiconductor hybrid nanostructured materials, and will have great applications in mass-production low-cost high performance photocatalysts.

4. Experimental section

4.1. Materials

All the reagents in this work are analytic grade and commercially available. Tin(II) chloride dehydrate ($\text{SnCl}_2 \cdot 2\text{H}_2\text{O}$), sodium hydroxide (NaOH), acetic acid (CH_3COOH), potassium permanganate (KMnO_4), phosphoric acid (H_3PO_4), hydrochloric acid (HCl), hydrogen peroxide (H_2O_2), sulfuric acid (H_2SO_4) and trisodium citrate dehydrate ($\text{Na}_3\text{C}_6\text{H}_5\text{O}_7 \cdot 2\text{H}_2\text{O}$) were purchased from China National Medicines Corporation Ltd, and the graphite was purchased from Sigma Aldrich. All the chemicals were used as received without further purification.

4.2. Synthesis

4.2.1. Preparation of GO nanosheets

GO was prepared from graphite using an improved synthesis method. Briefly, a mixture of concentrated $\text{H}_2\text{SO}_4\text{--H}_3\text{PO}_4$ (360: 40 mL) was added to a mixture of 3.0 g graphite flakes and 18.0 g KMnO_4 . The reaction was heated to 50°C and stirred for 12 h, then cooled to room temperature and poured onto ~ 350 g ice chips. Then, 3.0 mL of 30% H_2O_2 was slowly added to obtain a bright yellow dispersion. The suspension was then centrifuged ($4000 \times g$ for 4 h), and the supernatant was decanted away. The obtained deposit was washed repeatedly with deionized water and then dialyzed (molecular weight cutoff [MWCO] ~ 3000) for 2 weeks to obtain a clear dispersion of GO. Finally, the GO suspension was lyophilized at -60°C for 12 h.

4.2.2. Preparation of $\text{Sn}_3\text{O}_4/\text{rGO}$ heterostructure

In a typical experiment, 5 mg GO nanosheet, $\text{SnCl}_2 \cdot 2\text{H}_2\text{O}$ (0.90 g, 4.0 mmol) and $\text{Na}_3\text{C}_6\text{H}_5\text{O}_7 \cdot 2\text{H}_2\text{O}$ (2.94 g, 10 mmol) were dissolved in 10 mL of deionized water and stirred for 5 min. An aliquot of 10 mL of 0.2 M NaOH aqueous solution was added to the above solution while continuously stirring to obtain a homogeneous solution, which was then transferred to a 35 mL pressure reaction vials, which was heated to 180°C and maintained for 4 h using microwave synthesis system (CEM Discover SP). Then, the autoclave was cooled down to room temperature. The obtained composite nanotubes were washed with deionized water and ethanol to remove any ionic residual, then dried in an oven at 80°C for 4 h. For comparison, Sn_3O_4 nanosheets were also prepared in a similar fashion without the GO nanosheet.

4.3. Materials characterization

The XRD characterization was conducted on a PANalytical X'Pert3 Powder diffractometer equipped with a Cu target. The morphology and microstructure of the samples were examined by SEM-a Hitachi SU8020 microscopy. The TEM images were acquired on a FEI/Tecnai G2 F20 S-TWIN TMP microscope with an operating voltage of 200 kV. UV-vis

diffuse reflectance spectra (DRS) of the samples were recorded on a UV-vis spectrophotometer (UV-3600, Shimadzu) with an integrating sphere attachment within the range of 200–800 nm and with BaSO₄ as the reflectance standard. The XPS was collected on an ESCAlab MKII X-ray photoelectron spectrometer (K-Alpha 1063). Raman measurements were carried out using the LabRam HR Evolution system using the 532 nm line of an argon ion laser as the excitation source. Atomic force microscopy (AFM) was performed by means of a MFP-3D from Asylum Research. The PL spectra was measured with a Horiba Jobin Yvon (FluorMax 4) Luminescence Spectrometer under a laser excitation of 375 nm. The time-resolved PL decay curve was taken out with combined steady state and time resolved fluorescence spectrometer (FLS980, Edinburgh).

The H₂ evolution experiments were carried out in a gas-closed circulation system. In a typical reaction, the 100 mg catalyst powder was dispersed in CH₃OH aqueous solution using a magnetic stirrer (80 mL of distilled water + 20 mL of CH₃OH). A commercial solar simulator (300 W) equipped with a cut-off filter (λ > 420 nm) as the light source for photocatalytic H₂ generation. The H₂ evolution was measured with an on-line gas chromatograph (GC-7900).

Photoelectrode fabrication: the working electrode was fabricated by the fluorine-doped tin oxide (FTO) glass deposited with production samples. In a typical process of making a working electrode, 10 mg production sample was completely dispersed in a solution, which contained 5 mL water, 5 mL and 100 mL 5 wt% Nafion solution. The solution was ultrasonicated for 0.5 h to mark a homogeneous ink. Then 200 of ink with a pipettor was taken and spread onto FTO glass by dropwise to make an electrode catalyst. Finally, the photoelectrode was dried in air and then was ready for further characterization. A Cu wire was connected to the FTO substrate with the silver colloid paste. Finally, epoxy was solidified to cover the FTO substrate, the silver paste and the Cu wire to avoid short current in the measurement.

Photoelectrochemical measurement: photoelectrochemical analyses were carried out using a standard three-electrode cell with Ag/AgCl as reference electrode and Pt sheet as the counter electrode in the KCl solution (1 M). The electrolyte was bubbled with N₂ for 2 h to remove O₂. The light source used was identical with that used in the photocatalytic H₂ generation testing.

Acknowledgements

The work was supported by National Key R&D Program of China (2017YFE0102700) and the National Natural Science Foundation of China (No. 51372142, No. 21501090).

Appendix A. Supplementary data

Supplementary data associated with this article can be found, in the online version, at <https://doi.org/10.1016/j.apcatb.2018.01.055>.

References

- [1] M. Zhou, X.W.D. Lou, Y. Xie, *Nano Today* 8 (2013) 598–618.
- [2] Y. Xu, C. Zhang, P. Lu, X. Zhang, L. Zhang, J. Shi, *Nano Energy* 38 (2017) 484–503.
- [3] Z. Yue, A. Liu, C. Zhang, J. Huang, M. Zhu, Y. Du, P. Yang, *Appl. Catal. B- Environ.* 201 (2017) 202–210.
- [4] J.D. Xiao, Q. Shang, Y. Xiong, Q. Zhang, Y. Luo, S.H. Yu, H.L. Jiang, *Angew. Chem. Int. Ed.* 128 (2016) 9535–9539.
- [5] M. Lyu, J.H. Yun, P. Chen, M. Hao, L. Wang, *Adv. Energy Mater.* 7 (2017).
- [6] Z.F. Huang, J. Song, L. Pan, X. Zhang, L. Wang, J.J. Zou, *Adv. Mater.* 27 (2015) 5309–5327.
- [7] Q. Lu, Y. Yu, Q. Ma, B. Chen, H. Zhang, *Adv. Mater.* 28 (2016) 1917–1933.
- [8] N. Tian, Y. Zhang, X. Li, K. Xiao, X. Du, F. Dong, G.I. Waterhouse, T. Zhang, H. Huang, *Nano Energy* 38 (2017) 72–81.
- [9] F. Liang, Y. Zhu, *Appl. Catal. B- Environ.* 180 (2016) 324–329.
- [10] S. Wang, P. Chen, J.H. Yun, Y. Hu, L. Wang, *Angew. Chem. Int. Ed.* 129 (2017) 8620–8624.
- [11] X. Gao, H.B. Wu, L. Zheng, Y. Zhong, Y. Hu, X.W.D. Lou, *Angew. Chem. Int. Ed.* 126 (2014) 6027–6031.
- [12] S. Yin, X. Men, H. Sun, P. She, W. Zhang, C. Wu, W. Qin, X. Chen, *J. Mater. Chem. A* 3 (2015) 12016–12022.
- [13] M. Zhu, S. Kim, L. Mao, M. Fujitsuka, J. Zhang, X. Wang, T. Majima, *J. Am. Chem. Soc.* 139 (2017) 13234–13242.
- [14] Y. Zhu, Q. Ling, Y. Liu, H. Wang, Y. Zhu, *Appl. Catal. B- Environ.* 187 (2016) 204–211.
- [15] H. Feng, Z. Xu, L. Wang, Y. Yu, D. Mitchell, D. Cui, X. Xu, J. Shi, T. Sannomiya, Y. Du, *ACS Appl. Mater. Interfaces* 7 (2015) 27592–27596.
- [16] D. Liu, J. Wang, X. Bai, R. Zong, Y. Zhu, *Adv. Mater.* 28 (2016) 7284–7290.
- [17] H. Yu, L. Shang, T. Bian, R. Shi, G.I. Waterhouse, Y. Zhao, C. Zhou, L.Z. Wu, C.H. Tung, T. Zhang, *Adv. Mater.* 28 (2016) 5080–5086.
- [18] J. Chen, H.B. Yang, J. Miao, H.-Y. Wang, B. Liu, *J. Am. Chem. Soc.* 136 (2014) 15310–15318.
- [19] H. Huang, K. Xiao, Y. He, T. Zhang, F. Dong, X. Du, Y. Zhang, *Appl. Catal. B- Environ.* 199 (2016) 75–86.
- [20] X. Yu, X. Han, Z. Zhao, J. Zhang, W. Guo, C. Pan, A. Li, H. Liu, Z.L. Wang, *Nano Energy* 11 (2015) 19–27.
- [21] Z. Wang, W. Wu, Q. Xu, G. Li, S. Liu, X. Jia, Y. Qin, Z.L. Wang, *Nano Energy* 38 (2017) 518–525.
- [22] S. Chen, Z. Zhao, H. Liu, Charge transport at the metal-organic interface, *Annu. Rev. Phys. Chem.* 64 (2013) 221–245.
- [23] D.E. Schipper, Z. Zhao, A.P. Leitner, L. Xie, F. Qin, M.K. Alam, S. Chen, D. Wang, Z. Ren, R. Wang, *ACS Nano* 11 (2017) 4051–4059.
- [24] Z. Zhao, J. Tian, Y. Sang, A. Cabot, H. Liu, *Adv. Mater.* 27 (2015) 2557–2582.
- [25] L. Zhao, X. Chen, X. Wang, Y. Zhang, W. Wei, Y. Sun, M. Antonietti, M.M. Titirici, *Adv. Mater.* 22 (2010) 3317–3321.
- [26] Y. Zhu, Y. Wang, Q. Ling, Y. Zhu, *Appl. Catal. B- Environ.* 200 (2017) 222–229.
- [27] H. Shao, X. Zhao, Y. Wang, R. Mao, Y. Wang, M. Qiao, S. Zhao, Y. Zhu, *Appl. Catal. B- Environ.* 218 (2017) 810–818.
- [28] X. Li, X. Meng, J. Liu, D. Geng, Y. Zhang, M.N. Banis, Y. Li, J. Yang, R. Li, X. Sun, *Adv. Funct. Mater.* 22 (2012) 1647–1654.
- [29] D. Han, B. Jiang, J. Feng, Y. Yin, W. Wang, *Angew. Chem. Int. Ed.* 129 (2017) 7900–7904.
- [30] L. Sun, W. Wu, S. Yang, J. Zhou, M. Hong, X. Xiao, F. Ren, C. Jiang, *ACS Appl. Mater. Interfaces* 6 (2014) 1113–1124.
- [31] X. Yu, L. Wang, J. Zhang, W. Guo, Z. Zhao, Y. Qin, X. Mou, A. Li, H. Liu, *J. Mater. Chem. A* 3 (2015) 19129–19136.
- [32] L. Zhu, H. Lu, D. Hao, L. Wang, Z. Wu, L. Wang, P. Li, J. Ye, *ACS Appl. Mater. Interfaces* 9 (2017) 38537–38544.
- [33] M. Manikandan, T. Tanabe, P. Li, S. Ueda, G.V. Ramesh, R. Kodiyath, J. Wang, T. Hara, A. Dakshanamoorthy, S. Ishihara, *ACS Appl. Mater. Interfaces* 6 (2014) 3790–3793.
- [34] X. Yu, J. Zhang, Z. Zhao, W. Guo, J. Qiu, X. Mou, A. Li, J.P. Claverie, H. Liu, *Nano Energy* 16 (2015) 207–217.
- [35] S. Liu, L. Zheng, P. Yu, S. Han, X. Fang, *Adv. Funct. Mater.* 26 (2016) 3331–3339.
- [36] Q. Xiang, B. Cheng, J. Yu, *Angew. Chem. Int. Ed.* 54 (2015) 11350–11366.
- [37] J. Zhang, J. Yu, M. Jaroniec, J.R. Gong, *Nano Lett.* 12 (2012) 4584–4589.
- [38] X. Liu, J. Yang, W. Zhao, Y. Wang, Z. Li, Z. Lin, *Small* 12 (2016) 4077–4085.
- [39] F. Meng, S.K. Cushing, J. Li, S. Hao, N. Wu, *ACS Catal.* 5 (2015) 1949–1955.
- [40] A. Iwase, Y. Ng, R. Amal, A. Kudo, *J. Mater. Chem. A* 3 (2015) 8566–8570.
- [41] K. Iwashina, A. Iwase, Y.H. Ng, R. Amal, A. Kudo, *J. Am. Chem. Soc.* 137 (2015) 604–607.
- [42] C. Han, Z. Chen, N. Zhang, J.C. Colmenares, Y.J. Xu, *Adv. Funct. Mater.* 25 (2015) 221–229.
- [43] L. Xu, F. Zhang, X. Song, Z. Yin, Y. Bu, *J. Mater. Chem. A* 3 (2015) 5923–5933.
- [44] R. Liu, Y. Zhang, Z. Ning, Y. Xu, *Angew. Chem. Int. Ed.* 129 (2017) 15883–15888.
- [45] D. Voiry, J. Yang, J. Kupferberg, R. Fullon, C. Lee, H.Y. Jeong, H.S. Shin, M. Chhowalla, *Science* 353 (2016) 1413–1416.
- [46] W. Xu, M. Li, X. Chen, J. Zhao, R. Tan, R. Li, J. Li, W. Song, *Mater. Lett.* 120 (2014) 140–142.
- [47] G. Chen, S. Ji, Y. Sang, S. Chang, Y. Wang, P. Hao, J. Claverie, H. Liu, G. Yu, *Nanoscale* 7 (2015) 3117–3125.
- [48] Y. Hou, F. Zuo, A. Dagg, P. Feng, *Nano Lett.* 12 (2012) 6464–6473.
- [49] X. Yu, Z. Zhao, J. Zhang, W. Guo, L. Li, H. Liu, Z.L. Wang, *CrystEngComm* 19 (2017) 129–136.
- [50] F. Meng, J. Li, S.K. Cushing, M. Zhi, N. Wu, *J. Am. Chem. Soc.* 135 (2013) 10286–10289.
- [51] X. Yu, Z. Zhao, J. Zhang, W. Guo, J. Qiu, D. Li, Z. Li, X. Mou, L. Li, A. Li, *Small* 12 (2016) 2759–2767.
- [52] D.A. Wheeler, Y. Ling, R.J. Dillon, R.C. Fitzmorris, C.G. Dudzik, L. Zavodivker, T. Rajh, N.M. Dimitrijevic, G. Millhauser, C. Bardeen, *J. Phys. Chem. C* 117 (2013) 26821–26830.
- [53] W. Bi, X. Li, L. Zhang, T. Jin, L. Zhang, Q. Zhang, Y. Luo, C. Wu, Y. Xie, *Nat. Comm.* 6 (2015).
- [54] M.V. Dozzi, C. D'Andrea, B. Ohtani, G. Valentini, E. Sellie, *J. Phys. Chem. C* 117 (2013) 25586–25595.